Controllable inverse design of auxetic metamaterials using deep learning

Xiaoyang Zheng [a,b], Ta-Te Chen [a,b], Xiaofeng Guo [c], Sadaki Samitsu [b], Ikumu Watanabe [a,b,*]

[a] Graduate School of Pure and Applied Sciences, University of Tsukuba, 1-1-1 Tennodai, Tsukuba 305-8573, Japan
[b] Research Center for Structural Materials, National Institute for Materials Science, 1-2-1 Sengen, Tsukuba 305-0047, Japan
[c] School of Materials Science and Engineering, Southwest University of Science and Technology, Mianyang 621010, China

HIGHLIGHTS

- We propose an inverse design method for auxetic metamaterials using deep learning.
- We designed novel 2D auxetic metamaterials based on Voronoi tessellation for the training dataset.
- The trained neural network can generate 2D auxetic metamaterials with user-desired Young's moduli and Poisson's ratios.
- The proposed method can easily be extended to the inverse design of other architected materials.

GRAPHICAL ABSTRACT
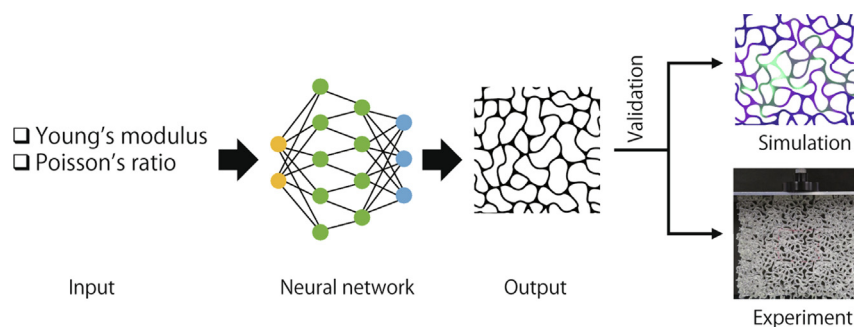
ABSTRACT

As typical mechanical metamaterials with negative Poisson's ratios, auxetic metamaterials exhibit counterintuitive auxetic behaviors that are highly dependent on their geometric arrangements. The realization of the geometric arrangement required to achieve a negative Poisson's ratio relies considerably on the experience of designers and trial-and-error approaches. This report proposes an inverse design method for auxetic metamaterials using deep learning, in which a batch of auxetic metamaterials with a user-defined Poisson's ratio and Young's modulus can be generated by a conditional generative adversarial network without prior knowledge. The network was trained based on supervised learning using a large number of geometrical patterns generated by Voronoi tessellation. The performance of the network was demonstrated by verifying the mechanical properties of the generated patterns using finite element method simulations and uniaxial compression tests. The successful realization of user-desired properties can potentially accelerate the inverse design and development of mechanical metamaterials.

© 2021 The Author(s). Published by Elsevier Ltd. This is an open access article under the CC BY license (http://creativecommons.org/licenses/by/4.0/).

1. Introduction

Auxetic metamaterials, which are mechanical metamaterials with negative Poisson's ratios, exhibit counterintuitive deformation behavior [1–7]. Under uniaxial compressive loading, auxetic metamaterials contract in the orthogonal directions rather than expanding; this behavior is in contrast to that of natural and synthetic materials, which have positive Poisson's ratios. Further, under bending loading, an auxetic metamaterial plate deforms into a convex shape, in contrast to the saddle shape usually seen for common materials. Compared with conventional materials, auxetic metamaterials have higher shear resistance, fracture resistance, indentation resistance, impact resistance, and energy absorption. Such distinctive behaviors make auxetic metamaterials promising candidates for developing impact absorbers [8,9], strain sensors [10,11], and actuators [12–14], as well as for applications in biomedicine [15,16] and electrochemical energy storage and conversion [17,18]. In addition, recent advances in additive manu-

* Corresponding author at: Research Center for Structural Materials, National Institute for Materials Science, 1-2-1 Sengen, Tsukuba 305-0047, Japan.
E-mail address: WATANABE.Ikumu@nims.go.jp (I. Watanabe).

facturing technologies have opened new avenues for the design and fabrication of such complicated structures [19,20].

Auxetic behavior can be quantified by the Poisson's ratio $v = -\varepsilon_t/\varepsilon_l$, where ε_t and ε_l are the transverse and longitudinal components of engineering strain, respectively, for a deformed material under a uniaxial load. For isotropic linear elastic materials, v must satisfy one of the following conditions [1]: $v \in [-1, 0.5]$ for three-dimensional (3D) materials and $v \in [-1, 1]$ for two-dimensional (2D) materials. Negative Poisson's ratio materials were founded in the 1980s [22–25]; since then, considerable efforts have been devoted designing, modeling, and analyzing auxetic metamaterials [26–29]. Despite such intensive efforts to design new auxetic metamaterials, it remains challenging to design flexible auxetic metamaterials with extreme properties, such as materials that can maintain negative Poisson's ratios consistently during large deformations [21,39,40,32]. For example, some delicately designed structures have positive Poisson's ratios under small deformations and only exhibit negative Poisson's ratios during further compression [39,40,32]. This is because of the limitations of conventional design methods. Forward design is the mainstream method for designing auxetic metamaterials and includes approaches such as bioinspired methods [30,31], mathematical control [32–35], topology optimization [36–38], and Boolean and lofting operations of simple geometries [39–43]. The forward design approach follows a general process: first, a structure is created, and its mechanical properties are then investigated by finite element method (FEM) simulations or mechanical testing (Fig. 1). The mechanical properties of the designed materials are known only after time-consuming simulations or experiments. In addition, because the properties of auxetic metamaterials are determined by the geometry and assembly of periodic unit cells, the traditional methods are highly dependent on the prior knowledge of experienced designers, resulting in a limited number of design spaces. Further, structural optimization techniques can be employed to achieve extreme properties such as negative Poisson's ratios even at finite strain [27,38]; however, nonlinear optimization remains challenging from the perspectives of robustness and efficiency.

Recent advances in deep learning have facilitated the inverse design of new materials using various artificial neural networks [44–53]. However, to the best of the authors' knowledge, deep learning has not yet been successfully harnessed to create novel auxetic metamaterials and rather has been used only to predict the mechanical behavior of specific auxetic configurations [48]. One important reason for this situation is that the properties of an auxetic metamaterial are almost completely determined by the geometry and assembly of periodic unit cells. The realization of a negative Poisson's ratio requires a delicate arrangement and

design of the unit cells; therefore, it is very difficult to build a large dataset consisting of thousands of geometries of auxetic metamaterials and their corresponding properties. For example, success has been achieved in previous studies only in the property prediction and pattern design of simple square-shaped cellular materials [44] or in the realization of isotropic elastic stiffness based on randomly generated architectures [47].

In this study, we devised a deep learning framework that can successfully generate auxetic metamaterials with assigned Young's moduli and Poisson's ratios. First, we created a large dataset composed of tens of thousands of geometric patterns and their corresponding mechanical properties. The patterns were derived from Voronoi tessellation, and their properties were calculated using a homogenization algorithm. The dataset was then used to train a conditional generative adversarial network (CGAN). Unlike a common generative adversarial network (GAN), which consists of a generator and discriminator, the CGAN uses a linear regression module (solver) to predict the properties of patterns from the generator. The discriminator was trained to push the generator to produce realistic patterns, and the solver was trained to push the generator to yield patterns with user-defined properties. After the CGAN had been well trained, it could rapidly generate new patterns with user-defined properties and could generate auxetic metamaterials with constantly negative Poisson's ratios during large deformations. Finally, the auxetic behaviors of the generated metamaterials were verified by FEM simulations and uniaxial compression tests.

2. Methods

2.1. Voronoi tessellation algorithm

As illustrated in Fig. 2, two-dimensional (2D) topology patterns were created using Voronoi tessellation, which is a robust method that is capable of creating various porous materials [54–59]. To ensure the periodicity of these 2D patterns, periodic boundary conditions were applied in the Voronoi tessellation. Briefly, a seed consisting of 64 coordinate points was initially created according to Mitchell's best candidate algorithm [60]. A 2D Voronoi diagram was created based on the seed. To mimic the nature of actual auxetic foams, which have both convex and concave cells [61], the 2D Voronoi diagram was modified by merging two adjacent polygons. Finally, a new pattern was formed after smoothing the edges of the polygons using Chaikin's algorithm because smooth surfaces have more homogeneous stress responses than sharp surfaces [62,63]. Note that the relative density of a pattern can be tuned easily by
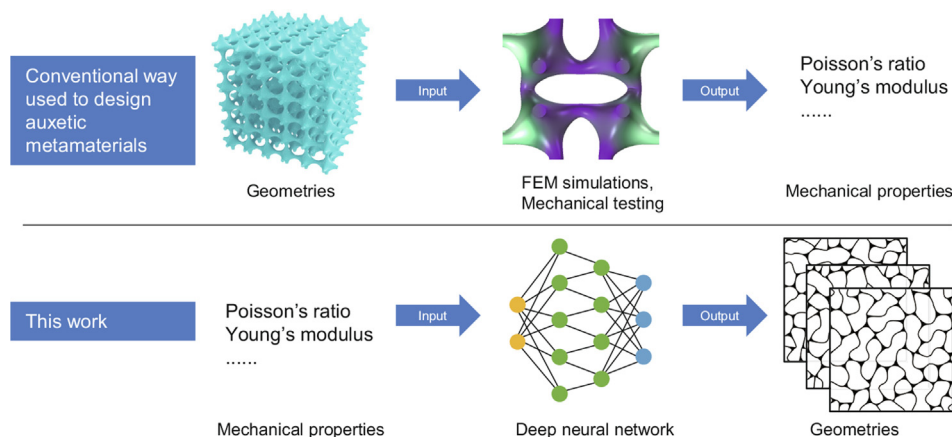

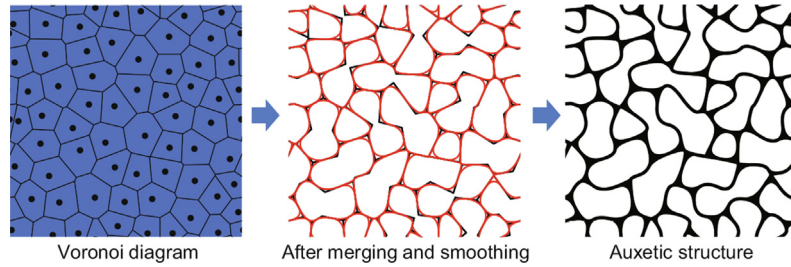**Fig. 1.** Comparison of the conventional design method and our method.

Fig. 2. Process of structure generation using Voronoi tessellation.

changing the width of the edges. Here, the width was fixed for simplicity. The relative density of the patterns was approximately 0.154. By repeating this process, an infinite number of different patterns can be created to facilitate big-data-driven material design.

2.2. Homogenization algorithm

The elastic moduli (Young's modulus and Poisson's ratio) were calculated according to the theory of homogenization, which has been used extensively to probe the equivalent linear elasticity of periodic composites [64–66]. According to the theory of homogenization, the effective elasticity tensor $\widetilde{C}_{ijkl}$ of a periodic pattern can be computed as:

$$\widetilde{C}_{ijkl} = \frac{1}{|V|} \int_V C_{pqrs} \left(\varepsilon_{pq}^{0(ij)} - \varepsilon_{pq}^{(ij)} \right) \left(\varepsilon_{rs}^{0(kl)} - \varepsilon_{rs}^{(kl)} \right) dV \tag{1}$$

where $|V|$ is the area of a square domain, C_{pqrs} is the locally varying stiffness tensor, $\varepsilon_{pq}^{0(ij)}$ represents the prescribed macroscopic strain fields (three strain fields in the case of two dimensions: horizontal, vertical, and shear strains), and $\varepsilon_{pq}^{(ij)}$ represents the locally varying strain fields and is defined as:

$$\varepsilon_{pq}^{(ij)} = \varepsilon_{pq}\left(\chi^{ij} \right) = \frac{1}{2} \left(\chi_{p,q}^{ij} + \chi_{q,p}^{ij} \right) \tag{2}$$

The locally varying strain fields are based on the displacement fields χ^{ij}, which can be determined using a prescribed macroscopic strain:

$$\int_V C_{ijpq} \varepsilon_{ij}(\upsilon) \varepsilon_{ij}\left(\chi^{kl} \right) dV = \int_V C_{ijpq} \varepsilon_{ij}(\upsilon) \varepsilon_{pq}^{0(kl)} dV, \forall \upsilon \in V \tag{3}$$

where υ denotes the virtual displacement field. The numerical homogenization procedure is discussed in more detail in the literature [64–66]. After obtaining the effective elasticity tensor $\widetilde{C}_{ijkl}$, the effective elastic moduli (i.e., Young's modulus, Poisson's ratio, shear modulus, and bulk modulus) can be calculated.

In this work, each pattern was first converted into a 256×256 element matrix consisting of 0 and 1, where 0 represents void regions and 1 represents solid regions. Subsequently, trial strain fields were applied to the element matrix to determine the reaction forces and stored elastic energy. Then, a homogenized elasticity tensor was obtained after the homogenization calculation. Finally, the effective elastic moduli of the patterns were calculated according to the elasticity tensor. The material model used in the homogenization was a linear elastic material with a Young's modulus of 0.6615 MPa and a Poisson's ratio of 0.49; these values were chosen to fit the equivalent elastic moduli of an incompressible neo-Hookean solid under a small deformation.

2.3. Dataset preparation

After topology creation and elastic modulus calculation, a large dataset was obtained, in which each datapoint consisted of a pattern and its corresponding labels (Poisson's ratio and Young's modulus). The training dataset was composed of 100,000 datapoints. Fig. 3(a) shows the 100,000 randomly created geometric patterns in the property space with the axes representing the Poisson's ratio (v) and Young's modulus (E). The randomly created patterns scattered in the material property space form a nearly triangular shape, with 2.1 kPa $< E <$ 13.7 kPa and $-0.28 < v < 0.38$. We refer to the triangular region as the available E–v space, in which random labels were sampled to train the neural network. Fig. 3(b) shows the distributions of the Poisson's ratios of these randomly created patterns. The distributions indicate that less than 3% of the randomly created patterns have negative Poisson's ratios.

2.4. Generative deep learning model

We devised a CGAN to train the created dataset. A GAN, which consists of two models (a generator and discriminator), is a type of deep learning network for data generation [67–69]. The generator and discriminator are trained simultaneously by an adversarial process, in which the generator learns to produce data with characteristics similar to those of the training data, whereas the discriminator learns to distinguish between real data and the generated data. A CGAN is a type of GAN in which conditional generation is realized by taking advantage of labels during the training process. However, with regard to precise data generation, the conventional CGAN can hardly provide good guidance for training the generator because the discriminator always suffers from overfitting [70]. We addressed this problem by employing an independent module (solver). The solver is a linear regression network that acts as a linear elasticity solver to predict the Young's modulus and Poisson's ratio of a given pattern (obtained from the dataset or generated by the CGAN). Fig. 4(a) illustrates the architecture of the proposed CGAN. A three-player game was conducted in which the generator deceived the discriminator in terms of geometry and simultaneously deceived the solver in terms of elastic moduli. After the CGAN had been well trained using 100,000 datapoints, it could generate a batch of patterns for a given label (Young's modulus and Poisson's ratio). More details on the CGAN are discussed in Appendix A.

2.5. Uniaxial compression tests

The auxetic behaviors of the generated metamaterials were first investigated using a set of 3D-printed samples in uniaxial compression tests. Each sample consisted of 3×3 unit cells and had overall dimensions of 120 mm $\times$ 120 mm $\times$ 15 mm. The unit cell number and size are sufficient to represent a periodic porous material [47]. To ensure that the specimens underwent large deformation without cracks, they were fabricated using an elastic photopolymer resin (Elastic 50A resin, Formlabs, USA) by employing a 3D printer (Form 3, Formlabs, USA). A subtle surface finish was achieved without the use of support structures. The printing parameters were as follows: a layer thickness of 0.05 mm and an
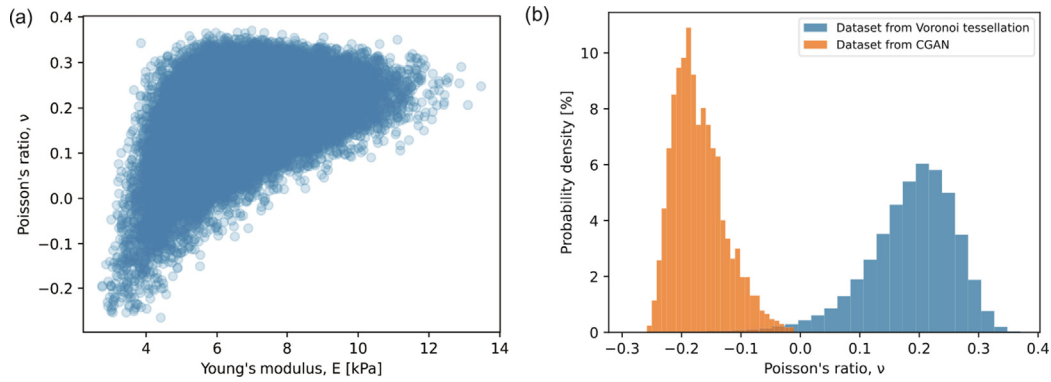
Fig. 3. Dataset for neural network training. (a) Young's moduli and Poisson's ratios of 100,000 randomly created patterns from Voronoi tessellation. (b) Distributions of Poisson's ratios for randomly created patterns and for CGAN-outputted patterns with an input condition of $v = -0.28$.
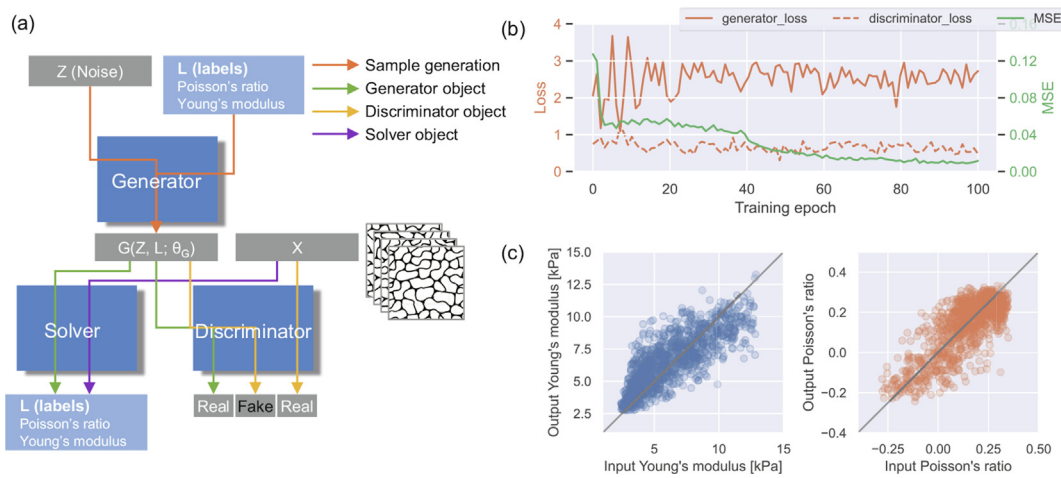

Fig. 4. Inverse design using CGAN. (a) CGAN architecture. (b) CGAN performance for different training datapoints. (c) Comparison between user-input and CGAN-output real elastic moduli.

operation temperature of 33 °C. All the specimens were fully cured at 60 °C for 20 min after washing with isopropanol. A typical 3D-printed sample is shown in Fig. 5(a).

The mechanical properties of the 3D-printed specimens were investigated by performing static compression tests using a motorized test stand (EMX-500 N, IMADA, Japan). A constant displacement rate of 10 mm/min was set during the tests, in which the samples were uniaxially compressed between two plates. The deformation process was captured using a high-speed camera, and the stress–strain curves were plotted using the recorded load–displacement data. The Hencky (logarithmic) strain components of the longitudinal (compression) and transverse directions were calculated using

$$\epsilon_i = \ln\left[1 + \frac{\bar{u}_i}{L_i}\right] = \ln\left[1 + \varepsilon_i\right] \quad \text{for } i \in \{l, t\}, \tag{4}$$

where $\bar{u}_i$ is the average boundary displacement between the top and bottom or the left and right of the red-marked interior unit cell, and L_i is the initial length of the interior unit cell. In this study, $L_l = L_t = 40$ mm. The average boundary displacements of the interior unit cell were measured by post-processing the recorded movies. Using the Hencky strain, Poisson's ratio at finite strain was defined as $v_{lt} = -\epsilon_t/\epsilon_l$.

The Young's modulus E_l for the longitudinal (compression) direction was calculated by linear fitting of the initial linear portions of the stress–strain curves. Least-squares approach was used to find the suitable value of E_l, in which the optimization problem was defined as

$$\min\left[\sum_{k=1}^{N}\left(\frac{F^{(k)}}{A} - \varepsilon^{(k)}E_l\right)^2\right], \tag{5}$$

where N is number of data, F is the applied load, and A is the initial contact area between the sample and the measuring instrument. In this study, the initial contact area was calculated as $A = 1,800$ mm^2 (120 mm × 15 mm).

In this study, compression tests were carried out on the structure in two directions, namely, x and y, as shown in Fig. 5(b); that is, $v_{xy}, v_{yx}, E_x,$ and E_y were evaluated.
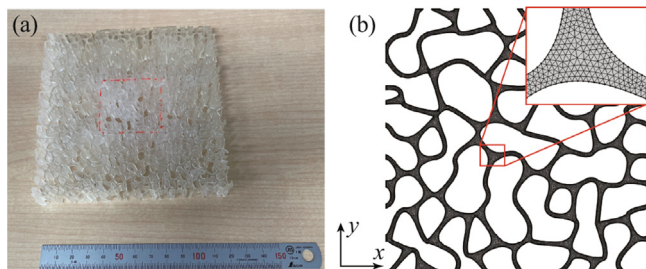

Fig. 5. Example of an evaluated object: (a) The 3D printed-sample and (b) a finite element meshing of an RVE.

2.6. Finite element method simulations

A deformation problem with a periodic microstructure, i.e., a representative volume element (RVE), was solved using a nonlinear FEM to simulate the deformation state at finite strain [31,71,72]. The displacement field $\boldsymbol{w}$ in an RVE is divided into the uniform part $\bar{\boldsymbol{u}}$ and the periodic part $\tilde{\boldsymbol{u}} : \boldsymbol{w} = \bar{\boldsymbol{u}} + \tilde{\boldsymbol{u}}$. The uniform displacement $\bar{\boldsymbol{u}}$ is described by the macroscopic displacement gradient $\bar{\boldsymbol{H}}$ as $\bar{\boldsymbol{u}} = \bar{\boldsymbol{H}}\boldsymbol{Y}$, where $\boldsymbol{Y}$ is the coordination system in the RVE. The boundary value problem of an RVE is formulated as a self-equilibrium problem for a periodic displacement field $\tilde{\boldsymbol{u}}$:

$$\int_{\Omega_Y} \boldsymbol{P} : \nabla_Y \tilde{\boldsymbol{\eta}} d\Omega_Y = 0 \quad \forall \tilde{\boldsymbol{\eta}} \in \boldsymbol{W}_{\text{periodic}}, \tag{6}$$

where $\boldsymbol{P}$ is first Piola–Kirchhoff stress, $\tilde{\boldsymbol{\eta}}$ is the variation of the periodic displacement $\tilde{\boldsymbol{u}}, \Omega_Y$ is the volume of the overall RVE, and $\boldsymbol{W}_{\text{periodic}}$ is the real solution space of the periodic function.

Based on the periodicity of the displacement field, the difference in displacements at two points A and B, which satisfy the periodicity on the corresponding surfaces of the RVE, is derived as $\boldsymbol{w}_A - \boldsymbol{w}_B = \bar{\boldsymbol{H}}(\boldsymbol{Y}_A - \boldsymbol{Y}_B)$. The above node-based boundary conditions are set on the finite element model of an RVE, and the displacement field $\boldsymbol{w}$ is then controlled by the macroscopic displacement gradient $\bar{\boldsymbol{H}}$. Following the definition of an RVE, a macroscopic variable can be calculated as the volume average of the corresponding microscopic variable. Thus, the macroscopic stress $\bar{\boldsymbol{P}}$ can be evaluated as

$$\bar{\boldsymbol{P}} := \frac{1}{\Omega_Y} \int_{\Omega_Y} \boldsymbol{P} d\Omega_Y. \tag{7}$$

Based on the above equations, the mechanical properties of the proposed patterns were further validated using an FEM simulation platform (COMSOL Multiphysics Ver. 5.4, COMSOL, Sweden). A 2D plane strain model was utilized under periodic boundary conditions. To mimic the properties of the 3D-printed material, the material model in the simulations was defined as an incompressible neo-Hookean model with a Young's modulus of 0.6615 MPa that was fitted from the compression tests. All the model geometries were meshed using approximately 2.5×10^5 second-order triangular solid elements. An example of meshing is shown in Fig. 5(b). A contact condition based on an augmented Lagrangian method was set in the finite element model. For the large deformation, a parametric sweep of the longitudinal displacement was used with a stop condition of $\varepsilon_l = 0.2$. The Poisson's ratios and Young's moduli in the simulation results were calculated using the same method that was employed to obtain the experimental results.

3. Results and discussion

3.1. Conditional generative adversarial network

We tested the performance of our CGAN model during each epoch by generating 1024 patterns with labels that were randomly sampled from the available E–v space. The performance was evaluated in terms of the mean squared error (MSE) of the sum of E and v:

$$\text{MSE} = \frac{1}{N} \sum_{i=1}^{N} \left\{ \left(E^{(i)} - \widehat{E}^{(i)} \right)^2 + \left(v^{(i)} - \hat{v}^{(i)} \right)^2 \right\}, \tag{8}$$

where $N = 1024$ is the number of labels sampled from the available E–v space, E is the normalized input Young's modulus, $\widehat{E}$ is the normalized output Young's modulus, v is the normalized input Poisson's ratio, and $\hat{v}$ is the normalized output Poisson's ratio. To facilitate deep learning, both the Young's modulus and Poisson's

ratio were normalized to the range from 0 to 1 based on the maximum and minimum values of the E–v space shown in Fig. 3(a). A smaller MSE indicates better performance. Fig. 4(b) shows the change in the MSE during the training epoch. Two convergence stages are observed in the MSE curve. The first one is before epoch 5, where the solver learns very rapidly to generate patterns similar to the real patterns. The next stage is $5 < \text{epoch} < 50$, where the solver learns relatively slowly to generate patterns with the corresponding input elastic moduli. Initially, the MSE decreases rapidly; then, it decreases gradually, finally reaching a minimum of approximately 0.014 after epoch 60. The low MSE indicates that our CGAN is capable of generating patterns with a user-defined Young's modulus and Poisson's ratio. In addition, the line plots for the loss (see Appendix A for the definition) of the generator and discriminator are shown in Fig. 4(b). The plots represent typical loss–epoch graphs of a stable GAN training process: the losses of the generator and discriminator begin erratically and gradually converge to a stable equilibrium after epoch 20. This finding further demonstrates the stability of our CGAN.

3.2. Inverse design of auxetic metamaterials

After the CGAN had been well trained using appropriate parameters, it could invert the design of auxetic metamaterials: a label (Young's modulus and Poisson's ratio) was input, and the CGAN generated a batch of geometrical patterns with the corresponding Young's modulus and Poisson's ratio. The performance of the trained CGAN was evaluated by comparing each input value and its output values (i.e., the Young's modulus and Poisson's ratio of the generated pattern). Fig. 4(c) compares 1024 samples with input labels sampled from the available E–v space. The coordinates of each point correspond to the input Young's modulus or Poisson's ratio (X coordinate) and the output Young's modulus or Poisson's ratio (Y coordinate). A position closer to the bisection line ($Y = X$) represents better performance of the CGAN. The narrow bandwidth of the scatter distributions indicates the good performance of the trained CGAN, demonstrating that the CGAN can generate a batch of geometries with user-desired Young's moduli and Poisson's ratios. These results also show that the CGAN can effectively perform extrapolation from the training data to provide a controllable inverse design, in contrast to the random generation obtained by Voronoi tessellation.

We further demonstrated that the trained CGAN facilitates the inverse design of auxetic metamaterials with very low negative Poisson's ratios. Considering that the lower boundary of the Poisson's ratio in the available E–v space had $v = -0.28$ and $E = 3$ kPa, we input the label with these values and the CGAN generated a batch of auxetic metamaterials (Fig. 6). In this figure, the input and output values are also compared below each pattern and show good agreement. Fig. 3(b) compares the distribution of Poisson's ratios between the CGAN-generated patterns and randomly created patterns. The comparison shows that it is easy to generate auxetic metamaterials with very low negative Poisson's ratios using the CGAN, in contrast to the random generation method. Although among the structures randomly generated with the Voronoi tessellation algorithm in Section 2.3, only 3% had a negative Poisson's ratio, the proposed approach can almost certainly generate the intended disordered structures having negative Poisson's ratios. More importantly, this inverse design method does not require delicate arrangement of the shapes, distributions, and combinations of geometrical elements. This method is independent of prior knowledge about the design of auxetic metamaterials. More patterns generated by the CGAN with different elastic moduli are shown in Figs. A3 and A4 in Appendix A.

Patterns generated by CGAN						
v(predict)	−0.30	−0.30	−0.30	−0.30	−0.30	−0.30
v(reference)	−0.2054	−0.2722	−0.1894	−0.2020	−0.2531	−0.2135
v_{xy}(FEM)	−0.1963	−0.25286	−0.1864	−0.2142	−0.23647	−0.2217
v_{yx}(FEM)	−0.1512	−0.1952	−0.1081	0.19325	−0.1801	−0.1609
E(predict), [MPa]	3000	3000	3000	3000	3000	3000
E(reference), [MPa]	3.2960	3.2041	2.9374	2.6422	3.4789	3.0119
E_y (FEM), [MPa]	4.3747	3.2900	4.9060	3.0127	3.6860	3.3455
E_x (FEM), [MPa]	3.2380	2.4420	3.1007	2.7202	2.7287	2.5266

Fig. 6. Auxetic metamaterials generated using the CGAN with input labels of $E = 3$ kPa and $v = -0.28$.

3.3. Investigation of auxetic behavior

To probe the auxetic behavior of the generated metamaterials under large deformation, we conducted a systematic analysis by performing uniaxial compression tests and FEM simulations. Fig. 7(a) shows a sequence of progressively deformed shapes of the generated auxetic metamaterials under four different levels of compressive engineering strain. The experimental and simulation results show a consistent deformation tendency wherein the metamaterial gradually contracts when compressed uniaxially along with the shrinkage of its interior holes. The overall shrinkage phenomenon proves that the metamaterial is an auxetic metamaterial with a negative Poisson's ratio. The progressively deformed shapes of other patterns with Poisson's ratios ranging from −0.2 to 0.3 are shown in Fig. A3; the patterns with a positive Poisson's ratio expand laterally when compressed uniaxially.

Fig. 7(b) presents a quantitative evaluation of Poisson's ratios under different compression strains. The transverse strains were determined from the average transverse strains of the interior unit cell to reduce the influence of the boundary conditions. The figure shows that the calculated Poisson's ratios monotonically decrease with increasing strain ($\varepsilon \leqslant 0.2$). A more detailed Poisson's ratio–strain curve obtained from the simulation results was also com-

pared with the curve obtained from the experimental results. Initially, the Poisson's ratio decreases; then, it gradually increases during compression because the empty space is insufficient, which causes the ligaments to bend when they are in contact with each other. Overall, the experimental and simulation results demonstrate that the negative Poisson's ratio can maintain a wide range of compressive strain ($\varepsilon = 0.2$). Notably, the training dataset was calculated by the homogenization algorithm at small strain. In this case, a negative Poisson's ratio can be attained in the small strain region, as expected; however, it does not necessarily maintain this ratio during a large deformation. It typically changes during deformation, as shown in Fig. 7(b). The proposed approach can generate a suitable structure if the training dataset is produced in consideration of finite strain and the objective is set as maintaining a negative Poisson's ration during a large deformation.

We also analyzed the stresses of the auxetic metamaterials during deformation. As shown in Fig. 7(c), the stress–strain curves exhibit good linearity. The lack of transformation from the linear elastic region to the plateau region indicates that the auxetic behavior of the designed metamaterials is a result not of buckling, but rather of ligament bending. It is noteworthy that the designed auxetic metamaterials are considerably different from typical buckling-induced auxetic metamaterials, whose stress–strain
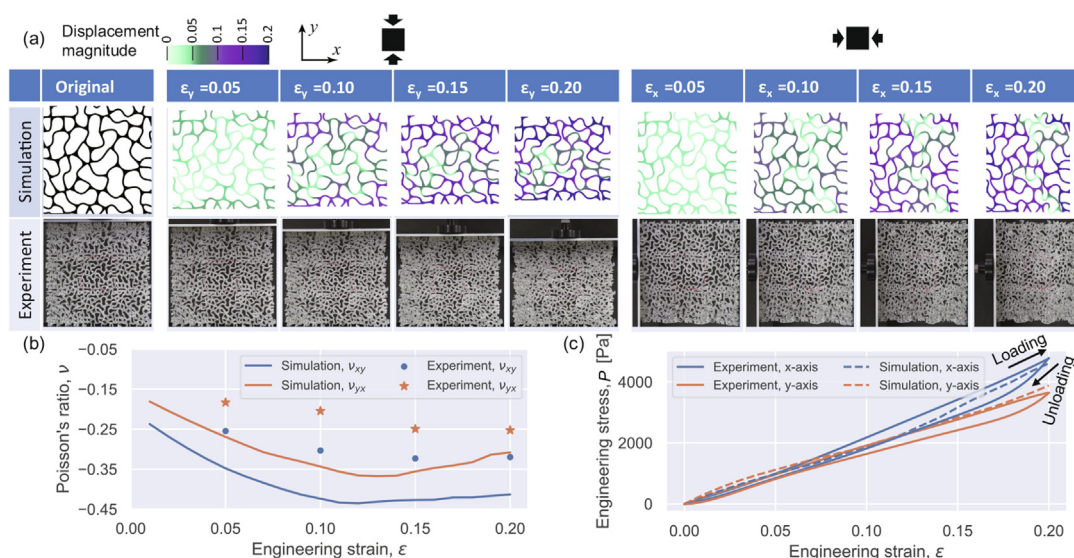

Fig. 7. Auxetic behavior of structures. (a) Progressively deformed configurations of FEM model and 3D-printed sample under uniaxial compressive load. (b) Poisson's ratio–strain curves and (c) stress–strain curves from FEM simulations and uniaxial compression tests.

curves have an additional plateau region between the linear elastic and densification regions [31,41–43].

4. Conclusions

We developed a controllable inverse design method for auxetic metamaterials using deep learning. The proposed deep learning model, CGAN, was trained using 100,000 randomly created patterns generated by Voronoi tessellation. The trained CGAN can facilitate the mass generation of 2D auxetic metamaterials with user-desired elastic moduli. The proposed method can be easily extended to the inverse design of 3D auxetic metamaterials in combination with Voronoi tessellation. In addition, this study opens new avenues to harness deep learning in the realization of user-desired properties for applications in which specific material properties are required (e.g., actuator fabrication, sensor manufacturing, and catalysis). Finally, although this work was focused only on 2D auxetic metamaterials with random structures, it is highly recommended that inverse design of 3D auxetic metamaterials be developed in future work, paving the way for further applications in which complicated 3D geometries are preferred.

Funding

Declaration of Competing Interest

The authors declare that they have no known competing financial interests or personal relationships that could have appeared to influence the work reported in this paper.

Acknowledgments

Appendix A. Details of conditional generative adversarial network

The CGAN used in this study was composed of three neural network structures: a generator, discriminator, and solver. The generator was trained to produce patterns of auxetic metamaterials from latent variables (multivariate normal distribution) and user-defined labels (Young's modulus and Poisson's ratio) and simultaneously aimed to deceive the discriminator and solver. The discriminator was trained to distinguish between the patterns produced by the generator and those from the real dataset. The solver was trained to predict the Young's modulus and Poisson's ratio of a given pattern. The CGAN was optimized by a minimax game using the following equations:

$$\hat{\theta}_D = \arg\min_{\theta_D}\{L_D(t_D, D(\mathbf{X}; \theta_D)) + L_D(u_D, D(G(\mathbf{Z}, \mathbf{L}; \theta_G); \theta_D))\} \quad (A.1)$$

$$\hat{\theta}_G = \arg\max_{\theta_G}\{L_D(u_D, D(G(\mathbf{Z}, \mathbf{L}; \theta_G); \theta_D)) - \alpha L_S(\mathbf{L}, S(G(\mathbf{Z}, \mathbf{L}; \theta_G); \theta_S))\}$$
$$(A.2)$$

$$\hat{\theta}_S = \arg\max_{\theta_S}\{L_S(\mathbf{L}, S(\mathbf{X}; \theta_S))\} \quad (A.3)$$

where θ_D, θ_G, and θ_S are the sets of parameters of the discriminator, generator, and solver, respectively. D, G, and S denote the discriminator, generator, and solver, respectively. $\mathbf{X} \in \mathbb{R}^{n \times p}$ is the training dataset (vectors of auxetic metamaterials), $\mathbf{L} \in \mathbb{R}^{n \times l}$ are the labels of the dataset $\mathbf{X}$ (i.e., Young's moduli and Poisson's ratios), and $\mathbf{Z} \in \mathbb{R}^{n \times l}$ are the latent variables from a multivariate normal distribution during each iteration. L_D is a loss function (binary cross-entropy function) for the discriminator. t_D and u_D are target labels and are generally set to 1 and 0, respectively. However, we applied the label smoothing technique for the target labels [73]: t_D was replaced by a random number between 0.7 and 1.2, and u_D was replaced by a random number between 0 and 0.3. The moderating weights, α, determined the extent to which the generator focused on the training of the input labels and was set to be 0.1 in our study.

Deep learning calculations were performed using TensorFlow [74]. An Adam optimizer with a learning rate of 0.0001 and $\beta 1$ of 0.5 was used to train the model. The batch size for the training was set to 32. The detailed network structures used in this study are listed in Tables A.1,A.2,A.3. In short, the layers used included a 2D convolutional layer, a 2D transposed convolutional layer, 2D max pooling, a fully connected layer, batch normalization, and dropout, and the activation functions used included Leaky ReLU and tanh. Note that circular padding was used in the 2D convolutional layer and 2D transposed convolutional layer to maintain and identify the periodicity of the patterns. Examples of down- and up-samplings with circular and zero paddings are shown in Fig. A1. This figure demonstrates that compared to the commonly used zero padding, circular padding can more effectively help the output tensor retain its periodicity.

Because the solver is independent of the generator and discriminator, we first trained the solver with supervised learning. The process took approximately 23 h to train 200 epochs with 100,000 datapoints on a single NVIDIA RTX A6000 graphic card. The solver is a type of linear regression model that can be used to predict the Young's modulus and Poisson's ratio (elastic moduli) of a given pattern. Fig. A2 shows the MSE between the predicted and reference elastic moduli for different numbers of datasets. A smaller MSE value represents a better performance of the trained solver. Each dataset was split as follows: 80% was used as the training set and 20% was used as the testing set. To prevent the solver from overfitting, early stopping was performed. As shown in Fig. A2(a), the MSE reaches a very low value of 0.003 after 20 epochs when using 100,000 datapoints, and it becomes difficult

Table A.1
Network architecture of generator.

Description	Kernel size	Resampling	Input shape	Output shape
Concatenate (Z, L)	-	-	128 + 2	130
Fully connected + Batch normalization + Reshape	-	-	130	4 × 4 × 512
2D transposed convolution + Batch normalization + Leaky ReLU	4 × 4	Up	4 × 4 × 512	8 × 8 × 256
2D transposed convolution + Batch normalization + Leaky ReLU	4 × 4	Up	8 × 8 × 256	16 × 16 × 128
2D transposed convolution + Batch normalization + Leaky ReLU	4 × 4	Up	16 × 16 × 128	32 × 32 × 64
2D transposed convolution + Batch normalization + Leaky ReLU	4 × 4	Up	32 × 32 × 64	64 × 64 × 32
2D transposed convolution + Batch normalization + Leaky ReLU	4 × 4	Up	64 × 64 × 32	128 × 128 × 16
2D transposed convolution	4 × 4	Up	128 × 128 ×16	256 × 256 × 1
Tanh	-	-	256 × 256 × 1	256 × 256 × 1

Table A.2
Network architecture of discriminator.

Description	Kernel size	Resampling	Input shape	Output shape
2D convolution + Leaky ReLU + Dropout	4 × 4	Down	256 × 256 × 1	128 × 128 × 16
2D convolution + Leaky ReLU + Dropout	4 × 4	Down	128 × 128 × 16	64 × 64 × 32
2D convolution + Leaky ReLU + Dropout	4 × 4	Down	64 × 64 × 32	32 × 32 × 64
2D convolution + Leaky ReLU + Dropout	4 × 4	Down	32 × 32 × 64	16 × 16 × 128
2D convolution + Leaky ReLU + Dropout	4 × 4	Down	16 × 16 × 128	8 × 8 × 256
2D convolution + Leaky ReLU + Dropout	4 × 4	Down	8 × 8 × 256	4 × 4 × 512
Flatten	-	-	4 × 4 × 512	8192
Fully connected	-	-	8192	1
Tanh	-	-	256 × 256 × 1	256 × 256 × 1

Table A.3
Network architecture of solver.

	Description	Kernel size/pool size	Resampling	Input shape	Output shape
Unit 1	2D convolution	3 × 3	-	256 × 256 × 1	256 × 256 × 16
	2D convolution	3 × 3	-	256 × 256 × 16	256 × 256 × 16
	2D max pooling	2 × 2	Down	256 × 256 × 1	128 × 128 × 16
Unit 2	2D convolution	3 × 3	-	128 × 128 × 16	128 × 128 × 32
	2D convolution	3 × 3	-	128 × 128 × 32	128 × 128 × 32
	2D max pooling	2 × 2	Down	128 × 128 × 32	64 × 64 × 32
Unit 3	2D convolution	3 × 3	-	64 × 64 × 32	64 × 64 × 64
	2D convolution	3 × 3	-	64 × 64 × 64	64 × 64 × 64
	2D max pooling	2 × 2	Down	64 × 64 × 64	32 × 32 × 64
Unit 4	2D convolution	3 × 3	-	32 × 32 × 64	32 × 32 × 128
	2D convolution	3 × 3	-	32 × 32 × 128	32 × 32 × 128
	2D max pooling	2 × 2	Down	32 × 32 × 128	16 × 16 × 128
Unit 5	2D convolution	3 × 3	-	16 × 16 × 128	16 × 16 × 256
	2D convolution	3 × 3	-	16 × 16 × 256	16 × 16 × 256
	2D max pooling	2 × 2	Down	16 × 16 × 256	8 × 8 × 256
Unit 6	2D convolution	3 × 3	-	8 × 8 × 256	8 × 8 × 384
	2D convolution	3 × 3	-	8 × 8 × 384	8 × 8 × 384
	2D max pooling	2 × 2	Down	8 × 8 × 384	4 × 4 × 384
Unit 7	2D convolution	3 × 3	-	4 × 4 × 384	4 × 4 × 512
	2D convolution	3 × 3	-	4 × 4 × 512	4 × 4 × 512
	2D max pooling	2 × 2	Down	4 × 4 × 512	2 × 2 × 512
Unit 8	2D convolution	3 × 3	-	2 × 2 × 512	2 × 2 × 512
	2D convolution	3 × 3	-	2 × 2 × 512	2 × 2 × 512
	2D max pooling	2 × 2	Down	2 × 2 × 512	1 × 1 × 512
	Flatten + Fully connected	-	-	1 × 1 × 512	256
	Fully connected			256	128
	Fully connected	-	-	128	2
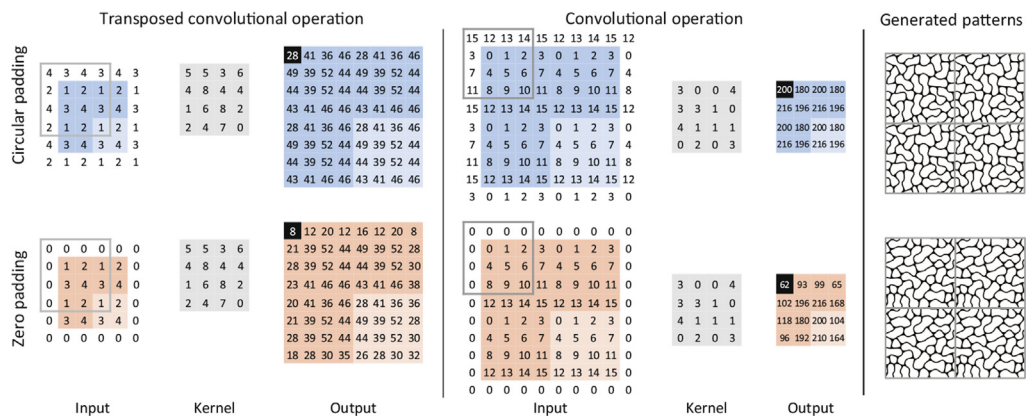
Fig. A1. Examples of the use of circular padding and zero padding. Compared to the patterns generated using zero padding, those produced using circular padding remain more periodic.
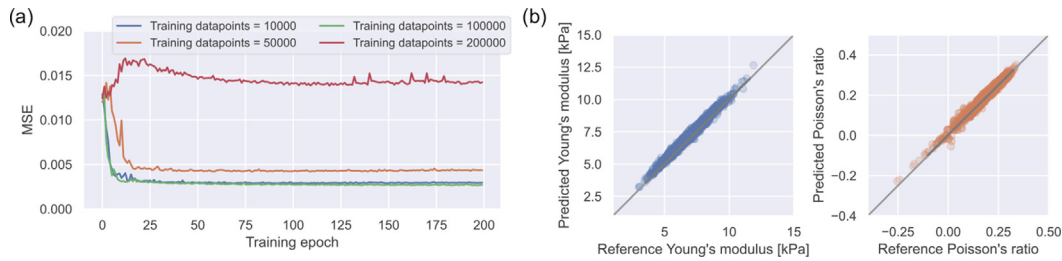
Fig. A2. (a) Performance of the solver evaluated using the MSE between the predicted and reference elastic moduli for different numbers of data points. (b) Comparison between the solver-predicted and reference elastic moduli. The latter are the elastic moduli of tested patterns calculated by the homogenization algorithm.

to decrease the MSE further even when using a larger dataset (e.g., 200,000 datapoints). To be conservative, we chose 100,000 data-points for the training process. Fig. A2(b) presents the predicted Young's moduli and Poisson's ratios of the tested patterns, in which the values predicted by the solver are close to the reference values, thus demonstrating the good performance of the solver. The linear relationship of the solver-predicted results is better than that of the CGAN-generated results. After the solver had been well trained, the checkpoints of the solver were saved and the solver was used to train the generator and discriminator, in which the saved check-points were used to calculate the loss of the patterns produced by the generator. The process spent approximately 35 h to train 200 epochs on a single NVIDIA RTX A6000 graphic card.

Appendix B. Patterns generated by CGAN

The well-trained CGAN is capable of generating numerous pat-terns with a user-defined Young's modulus and Poisson's ratio.

Fig. A3 shows some patterns produced by the CGAN with different Young's moduli and Poisson's ratios. The results show that the val-ues of the input elastic moduli are very close to those of the output elastic moduli, which further demonstrates the good performance of the CGAN. Note that the differences between the elastic moduli calculated by the homogenization algorithm and the FEM simula-tion are caused by the algorithms themselves. The close agreement among the results of the CGAN predictions, FEM simulations, and experiments confirms that the proposed CGAN-based technique is a robust method for the inverse design of auxetic metamaterials.

We also investigated the deformation behaviors of different CGAN-generated patterns under uniaxial compression (Fig. A4). The good curve fitting of the stress–strain curves and Poisson's ratio curves along the x- and y-axes demonstrates the isotropic properties of this type of pattern. Furthermore, some patterns that initially have positive Poisson's ratios exhibit auxetic behavior dur-ing further compression, which is caused by the shrinking of inte-rior concave pores.

Patterns generated by CGAN $\uparrow y \rightarrow x$						
v_i (input)	−0.2	−0.1	0	0.1	0.2	0.3
v_o (output)	−0.2029	−0.1004	0.0106	0.1091	0.2052	0.3028
v_{xy} (FEM)	−0.1891	−0.0710	0.0121	0.0735	0.1701	0.3125
v_{yx} (FEM)	−0.1312	−0.0975	0.0128	0.0896	0.1749	0.3483
E_i (input), [kPa]	4.0	4.5	5.0	5.5	6.0	8.5
E_o (output), [kPa]	3.9856	4.5753	4.9266	5.5892	5.8316	8.3386
E_y (FEM), [kPa]	3.9046	5.1088	3.8596	4.7835	5.8519	8.1307
E_x (FEM), [kPa]	3.8074	3.7126	5.5629	5.6258	5.8127	8.9898

Fig. A3. Patterns generated by the CGAN with different Young's moduli and Poisson's ratios.
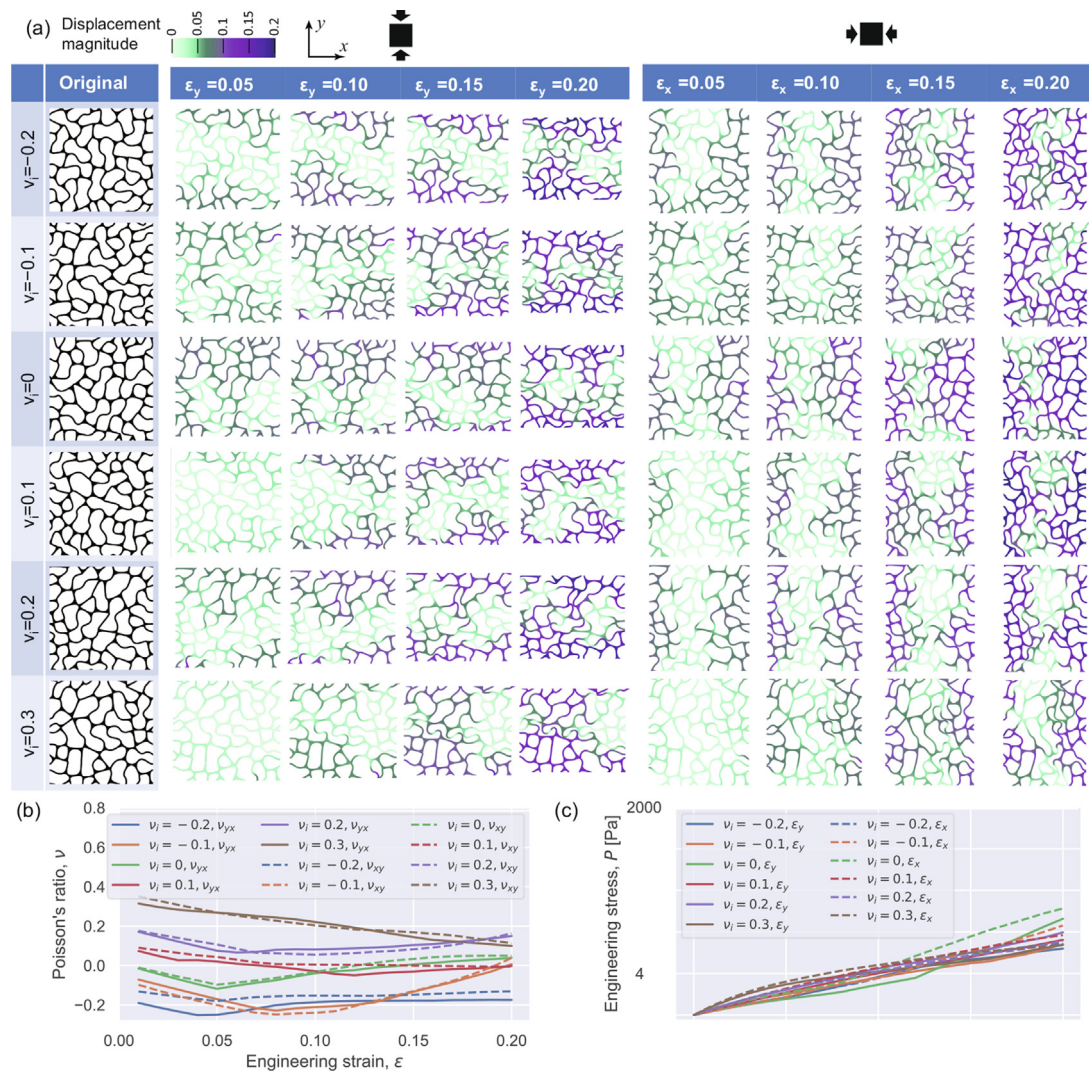
Fig. A4. Deformation behavior of patterns with different elastic moduli. (a) Progressively deformed configurations of FEM model under uniaxial compressive loading. (b) Poisson's ratio–strain curves and (c) stress–strain curves from FEM simulations.

References

[1] G.N. Greaves, A. Greer, R.S. Lakes, T. Rouxel, Poisson's ratio and modern materials, Nat. Mater. 10 (11) (2011) 823–837.

[2] R.S. Lakes, Negative-Poisson's-ratio materials: Auxetic solids, Annu. Rev. Mater. Res. 47 (2017) 63–81.

[3] X. Yu, J. Zhou, H. Liang, Z. Jiang, L. Wu, Mechanical metamaterials associated with stiffness, rigidity and compressibility: A brief review, Prog. Mater Sci. 94 (2018) 114–173.

[4] Z. Wang, C. Luan, G. Liao, J. Liu, X. Yao, J. Fu, Progress in auxetic mechanical metamaterials: Structures, characteristics, manufacturing methods, and applications, Adv. Eng. Mater. 22 (10) (2020) 2000312.

[5] Y. Liu, H. Hu, A review on auxetic structures and polymeric materials, Scientific Research and Essays 5 (10) (2010) 1052–1063.

[6] P.U. Kelkar, H.S. Kim, K.-H. Cho, J.Y. Kwak, C.-Y. Kang, H.-C. Song, Cellular auxetic structures for mechanical metamaterials: A review, Sensors 20 (11) (2020) 3132.

[7] D. Mousanezhad, B. Haghpanah, R. Ghosh, A.M. Hamouda, H. Nayeb-Hashemi, A. Vaziri, Elastic properties of chiral, anti-chiral, and hierarchical honeycombs: A simple energy-based approach, Theoretical and Applied Mechanics Letters 6 (2) (2016) 81–96.

[8] S. Yuan, F. Shen, J. Bai, C.K. Chua, J. Wei, K. Zhou, 3D soft auxetic lattice structures fabricated by selective laser sintering: TPU powder evaluation and process optimization, Materials & Design 120 (2017) 317–327.

[9] D.H. Le, Y. Xu, M.M. Tentzeris, S. Lim, Transformation from 2D meta-pixel to 3D meta-pixel using auxetic kirigami for programmable multifunctional electromagnetic response, Extreme Mechanics Letters 36 (2020) 100670.

[10] Y. Jiang, Z. Liu, N. Matsuhisa, D. Qi, W.R. Leow, H. Yang, J. Yu, G. Chen, Y. Liu, C. Wan, et al., Auxetic mechanical metamaterials to enhance sensitivity of stretchable strain sensors, Adv. Mater. 30 (12) (2018) 1706589.

[11] Y.-J. Lee, S.-M. Lim, S.-M. Yi, J.-H. Lee, S.-G. Kang, G.-M. Choi, H.N. Han, J.-Y. Sun, I.-S. Choi, Y.-C. Joo, Auxetic elastomers: Mechanically programmable meta-elastomers with an unusual Poisson's ratio overcome the gauge limit of a capacitive type strain sensor, Extreme Mechanics Letters 31 (2019) 100516.

[12] A. Lazarus, P.M. Reis, Soft actuation of structured cylinders through auxetic behavior, Adv. Eng. Mater. 17 (6) (2015) 815–820.

[13] J.I. Lipton, R. MacCurdy, Z. Manchester, L. Chin, D. Cellucci, D. Rus, Handedness in shearing auxetics creates rigid and compliant structures, Science 360 (6389) (2018) 632–635.

[14] K.K. Dudek, R. Gatt, J.N. Grima, 3D composite metamaterial with magnetic inclusions exhibiting negative stiffness and auxetic behaviour, Materials & Design 187 (2020) 108403.

[15] H.M. Kolken, S. Janbaz, S.M. Leeflang, K. Lietaert, H.H. Weinans, A.A. Zadpoor, Rationally designed meta-implants: A combination of auxetic and conventional meta-biomaterials, Materials Horizons 5 (1) (2018) 28–35.

[16] A.A. Zadpoor, Mechanical performance of additively manufactured meta-biomaterials, Acta Biomater. 85 (2019) 41–59.

[17] L. Weng, J. Zhou, R. Cai, Analytical model of li-ion diffusion-induced stress in nanowire and negative Poisson's ratio electrode under different operations, Int. J. Mech. Sci. 141 (2018) 245–261.

[18] P. Chang, H. Mei, Y. Tan, Y. Zhao, W. Huang, L. Cheng, A 3D-printed stretchable structural supercapacitor with active stretchability/flexibility and remarkable volumetric capacitance, Journal of Materials Chemistry A 8 (27) (2020) 13646–13658.

[19] X. Xin, L. Liu, Y. Liu, J. Leng, 4D printing auxetic metamaterials with tunable, programmable, and reconfigurable mechanical properties, Adv. Funct. Mater. 30 (43) (2020) 2004226.

[20] M.H. Yousuf, W. Abuzaid, M. Alkhader, 4D printed auxetic structures with tunable mechanical properties, Additive Manufacturing 35 (2020) 101364.

[21] K. Bertoldi, V. Vitelli, J. Christensen, M. Van Hecke, Flexible mechanical metamaterials, Nature Reviews Materials 2 (11) (2017) 1–11.

[22] I. Gibson, M.F. Ashby, The mechanics of three-dimensional cellular materials, Proceedings of the royal society of London. A. Mathematical and Physical Sciences 382 (1782) (1982) 43–59.

[23] F. Robert, An isotropic three-dimensional structure with Poisson's ratio = -1, J. Elast. 15 (1985) 427–430.

[24] A. Kolpakov, Determination of the average characteristics of elastic frameworks, Journal of Applied Mathematics and Mechanics 49 (6) (1985) 739–745.

[25] K. Wojciechowski, Constant thermodynamic tension Monte Carlo studies of elastic properties of a two-dimensional system of hard cyclic hexamers, Mol. Phys. 61 (5) (1987) 1247–1258.

[26] T. Strek, P. Kedziora, B. Maruszewski, A. Pozniak, K. Tretiakov, K. Wojciechowski, Finite element analysis of auxetic obstacle deformation and fluid flow in a channel, J. Non-Cryst. Solids 355 (24–27) (2009) 1387–1392.

[27] T. Strek, H. Jopek, E. Idczak, K.W. Wojciechowski, Computational modelling of structures with non-intuitive behaviour, Materials 10 (12) (2017) 1386.

[28] T.-C. Lim, Auxetic materials and structures, Springer, 2015.

[29] T.-C. Lim, Mechanics of metamaterials with negative parameters, Springer Nature (2020).

[30] J.A. Rosewitz, H.A. Choshali, N. Rahbar, Bioinspired design of architected cement-polymer composites, Cement and Concrete Composites 96 (2019) 252–265.

[31] D. Li, X. Bu, Z. Xu, Y. Luo, H. Bai, Bioinspired multifunctional cellular plastics with a negative Poisson's ratio for high energy dissipation, Adv. Mater. 32 (33) (2020) 2001222.

[32] X. Zheng, X. Guo, I. Watanabe, A mathematically defined 3D auxetic metamaterial with tunable mechanical and conduction properties, Materials & Design 198 (2021) 109313.

[33] C. Soyarslan, V. Blümer, S. Bargmann, Tunable auxeticity and elastomechanical symmetry in a class of very low density core-shell cubic crystals, Acta Mater. 177 (2019) 280–292.

[34] X. Zheng, Z. Fu, K. Du, C. Wang, Y. Yi, Minimal surface designs for porous materials: From microstructures to mechanical properties, J. Mater. Sci. 53 (14) (2018) 10194–10208.

[35] T. Strek, H. Jopek, K.W. Wojciechowski, The influence of large deformations on mechanical properties of sinusoidal ligament structures, Smart Mater. Struct. 25 (5) (2016) 054002.

[36] D.W. Abueidda, Z. Kang, S. Koric, K.A. James, I.M. Jasiuk, Topology optimization for three-dimensional elastoplastic architected materials using a path-dependent adjoint method, Int. J. Numer. Meth. Eng. 122 (8) (2021) 1889–1910.

[37] H.T. Kollmann, D.W. Abueidda, S. Koric, E. Guleryuz, N.A. Sobh, Deep learning for topology optimization of 2D metamaterials, Materials & Design 196 (2020) 109098.

[38] S. Czarnecki, T. Łukasiak, T. Lewiński, The isotropic and cubic material designs. recovery of the underlying microstructures appearing in the least compliant continuum bodies, Materials 10 (10) (2017) 1137.

[39] S. Babaee, J. Shim, J.C. Weaver, E.R. Chen, N. Patel, K. Bertoldi, 3D soft metamaterials with negative Poisson's ratio, Adv. Mater. 25 (36) (2013) 5044–5049.

[40] J.T. Overvelde, S. Shan, K. Bertoldi, Compaction through buckling in 2D periodic, soft and porous structures: Effect of pore shape, Adv. Mater. 24 (17) (2012) 2337–2342.

[41] L. Zhou, X. Zheng, K. Du, X. Guo, Q. Yin, A. Lu, Y. Yi, Parametric and experiment studies of 3D auxetic lattices based on hollow shell cuboctahedron, Smart Mater. Struct. 30 (2) (2021) 025042.

[42] C.S. Ha, M.E. Plesha, R.S. Lakes, Chiral three-dimensional isotropic lattices with negative Poisson's ratio, Physica Status Solidi (B) 253 (7) (2016) 1243–1251.

[43] T. Li, Y. Chen, X. Hu, Y. Li, L. Wang, Exploiting negative Poisson's ratio to design 3D-printed composites with enhanced mechanical properties, Materials & Design 142 (2018) 247–258.

[44] C. Ma, Z. Zhang, B. Luce, S. Pusateri, B. Xie, M.H. Rafiei, N. Hu, Accelerated design and characterization of non-uniform cellular materials via a machine-learning based framework, npj Computational Materials 6 (1) (2020) 1–8.

[45] P. Jiao, A.H. Alavi, Artificial intelligence-enabled smart mechanical metamaterials: Advent and future trends, Int. Mater. Rev. (2020) 1–29.

[46] B. Kim, S. Lee, J. Kim, Inverse design of porous materials using artificial neural networks, Science Advances 6 (1) (2020) eaax9324.

[47] Y. Mao, Q. He, X. Zhao, Designing complex architectured materials with generative adversarial networks, Science Advances 6 (17) (2020) eaaz4169.

[48] J.K. Wilt, C. Yang, G.X. Gu, Accelerating auxetic metamaterial design with deep learning, Adv. Eng. Mater. 22 (5) (2020) 1901266.

[49] J. Jiang, M. Chen, J.A. Fan, Deep neural networks for the evaluation and design of photonic devices, Nature Reviews Materials (2020) 1–22.

[50] S. Ye, B. Li, Q. Li, H.-P. Zhao, X.-Q. Feng, Deep neural network method for predicting the mechanical properties of composites, Appl. Phys. Lett. 115 (16) (2019) 161901.

[51] J. Pan, Y.-F. Zhang, J. Zhang, H. Banjade, J. Yu, L. Yu, S. Du, A. Ruzsinszky, Z. Hu, Q. Yan, Auxetic two-dimensional transition metal selenides and halides, npj Computational Materials 6 (1) (2020) 1–6.

[52] A. Yamanaka, R. Kamijyo, K. Koenuma, I. Watanabe, T. Kuwabara, Deep neural network approach to estimate biaxial stress-strain curves of sheet metals, Materials & Design 195 (2020) 108970.

[53] K. Koenuma, A. Yamanaka, I. Watanabe, T. Kuwabara, Estimation of texture-dependent stress-strain curve and r-value of aluminum alloy sheet using deep learning, Mater. Trans. 61 (12) (2020) 2276–2283.

[54] X. Zheng, X. Guo, Y. Yang, Z. Fu, K. Du, C. Wang, Y. Yi, Structure-dependent analysis of nanoporous metals: Clues from mechanical, conduction, and flow properties, The Journal of Physical Chemistry C 122 (29) (2018) 16803–16809.

[55] S. Zhao, T.M. Evans, X. Zhou, Three-dimensional Voronoi analysis of monodisperse ellipsoids during triaxial shear, Powder Technol. 323 (2018) 323–336.

[56] C. Zhang, S. Zhao, J. Zhao, X. Zhou, Three-dimensional Voronoi analysis of realistic grain packing: An XCT assisted set Voronoi tessellation framework, Powder Technol. 379 (2021) 251–264.

[57] Y. Yi, X. Zheng, Z. Fu, C. Wang, X. Xu, X. Tan, Multi-scale modeling for predicting the stiffness and strength of hollow-structured metal foams with structural hierarchy, Materials 11 (3) (2018) 380.

[58] K.A. Hart, J.J. Rimoli, Generation of statistically representative microstructures with direct grain geometry control, Comput. Methods Appl. Mech. Eng. 370 (2020) 113242.

[59] H. Ma, X. Zheng, X. Luo, Y. Yi, F. Yang, Simulation and analysis of mechanical properties of silica aerogels: From rationalization to prediction, Materials 11 (2) (2018) 214.

[60] T.J. Mitchell, An algorithm for the construction of D–optimal experimental designs, Technometrics 42 (1) (2000) 48–54.

[61] D. Li, L. Dong, R.S. Lakes, The properties of copper foams with negative Poisson's ratio via resonant ultrasound spectroscopy, Physica Status Solidi (B) 250 (10) (2013) 1983–1987.

[62] X. Guo, X. Zheng, Y. Yang, X. Yang, Y. Yi, Mechanical behavior of TPMS-based scaffolds: A comparison between minimal surfaces and their lattice structures, SN Applied Sciences 1 (10) (2019) 1–11.

[63] G.M. Chaikin, An algorithm for high-speed curve generation, Computer Graphics and Image Processing 3 (4) (1974) 346–349.

[64] K. Suzuki, N. Kikuchi, A homogenization method for shape and topology optimization, Comput. Methods Appl. Mech. Eng. 93 (3) (1991) 291–318.

[65] B. Said, M. Salah, T. Kanit, F. Kamel, On the homogenization of 2D porous material with determination of RVE, International Journal of Mechanical and Mechatronics Engineering 16 (1) (2016) 81–86.

[66] E. Andreassen, C.S. Andreasen, How to determine composite material properties using numerical homogenization, Comput. Mater. Sci. 83 (2014) 488–495.

[67] I. Goodfellow, J. Pouget-Abadie, M. Mirza, B. Xu, D. Warde-Farley, S. Ozair, A. Courville, Y. Bengio, Generative adversarial nets, Advances in Neural Information Processing Systems 27 (2014).

[68] T. Karras, S. Laine, T. Aila, A style-based generator architecture for generative adversarial networks, in: Proceedings of the IEEE/CVF Conference on Computer Vision and Pattern Recognition, 2019, pp. 4401–4410.

[69] P. Isola, J.-Y. Zhu, T. Zhou, A.A. Efros, Image-to-image translation with conditional adversarial networks, in: Proceedings of the IEEE Conference on Computer Vision and Pattern Recognition, 2017, pp. 1125–1134.

[70] M. Lee, J. Seok, Controllable generative adversarial network, IEEE Access 7 (2019) 28158–28169.

[71] I. Watanabe, A. Yamanaka, Voxel coarsening approach on image-based finite element modeling of representative volume element, Int. J. Mech. Sci. 150 (2019) 314–321.

[72] I. Watanabe, D. Setoyama, N. Nagasako, N. Iwata, K. Nakanishi, Multiscale prediction of mechanical behavior of ferrite–pearlite steel with numerical material testing, Int. J. Numer. Meth. Eng. 89 (7) (2012) 829–845.

[73] T. Salimans, I. Goodfellow, W. Zaremba, V. Cheung, A. Radford, X. Chen, Improved techniques for training GANs, Advances in Neural Information Processing Systems 29 (2016) 2234–2242.

[74] M. Abadi, P. Barham, J. Chen, Z. Chen, A. Davis, J. Dean, M. Devin, S. Ghemawat, G. Irving, M. Isard, et al., Tensorflow: A system for large-scale machine learning, in: 12th USENIX Symposium on Operating Systems Design and Implementation (OSDI 16), 2016, pp. 265–283.